 CMC, vol.14, no.2, pp.99-123, 2009

Studies of Texture Gradients in the Localized Necking Band of AA5754 by EBSD and Microstructure-Based Finite Element Modeling

Xiaohua Hu[1], Gordana A. Cingara[1], David S. Wilkinson[1], Mukesh Jain[2] Peidong Wu[2] and Raja K. Mishra[3]

Abstract: This work aims to understand the texture distribution in the localized necking band formed during uni-axial tension of AA5754 using an edge-constrained, plane strain post-necking FE model. The model domain is a long cross section of the band. Initial grain structure is mapped into the mesh from EBSD data using a modified Voroni-cell interpolation and considering pre-straining prior to localized necking. The material points in grains are assumed to exhibit isotropic elastoplastic behavior but have a relative strength in terms of Taylor factors which are updated by a Taylor-Bishop-Hill model. The predicted textures and gradients within the localized necking band correlate well with experimental measurements where large rigid body rotation and lattice spin are experienced due to geometric constraints and excessive deformation in the band.

Keywords: Localized necking, texture gradient, EBSD, finite element modeling

1 Introduction

The material texture and its evolution have received a lot of attentions through the years, as they can cause plastic anisotropy during deformation which in turn influences material formability and can lead to problems such as earing, surface roughening, roping, premature localization and fracture (Bronkhorst et al.,2007; Hu et al.,2008a; Hu et al.,2008b; Li et al.,2001; Wu et al.,2003; Wu et al.,2004; Yoon et al.,1999). Approaches to the prediction of texture evolution during deformation include the mean field methodologies which makes some simplifying assumptions such as Taylor (Van Houtte et al.,2005), Sachs-type (Leffers et al.,1989) or self-consistent (Lebensohn et al.,1993) schemes. The more recent advanced versions of

[1] Department of Materials Science and Engineering, McMaster University, Hamilton, Ont., Canada L8S 4L7
[2] Department of Mechanical Engineering, McMaster University, Hamilton, Ont., Canada L8S 4L7
[3] General Motors Research and Development Center, Warren, MI 48090-9055, USA

these schemes can give good prediction of texture and its evolution during uniform deformation. The predictions, however, are unsuccessful once shear localization starts. For example, the evolution of texture during simple shearing of an AA3004 alloy, previously cold rolled with a shear angle of 60^o, was shown to be much slower than that predicted by fully constrained – Taylor (FC-Taylor) or Advanced Lamel (ALAMEL) model (Hu et al.,2005b). This is because a macroscopic shear band is triggered by the sample corner tensile stresses at early deformation due to texture and microstructure softening (Hu et al.,2005a; Hu et al.,2005b). The excessive deformation in the very narrow band (below 10 μm in width) contributes to the major part of the average shear deformation across the shear zone of about 2 mm wide, while little deformation is in the region outside the band. A multi-scale procedure which involves a finite element model and a Taylor-type mean field scheme is able to capture the slow texture evolution by summing up the texture of different deformation regions with a weighting factor. Once a macroscopic shear band is formed, the deformation and fracture of the material is controlled by the material behavior within the band. Therefore, it is useful to understand the changes of texture in the band after the onset of localized necking.

Compared with the mean field approaches, microstructure-based crystal plasticity finite element models (Bate,1999; Becker,1991; Becker,1992; Delannay et al.,2006; Kalidindi et al.,1992; Wu et al.,2007) can treat not only the statistical texture, but also the spatial distribution of grain orientations measured experimentally, e.g., by EBSD technique. The stress and strain compatibility is guaranteed and heterogeneity of deformation between grains and within grains can be calculated. Bronkhorst et al. has studied the microstructure and texture evolution of polycrystalline metallic materials under localization conditions (Bronkhorst et al.,2007) in top hat samples.

Based on the analysis of geometric effects on instability sequence for uniaxial tension, a two-stage modeling procedure has been developed to study the localization behavior (Hu et al.,2008a). A plane stress model was used to study the pre-necking behavior, i.e., from uniform deformation to the onset of localized necking (Hu et al.,2008a; Hu et al.,2007; Hu et al.,2008b). An edge-constrained plane strain model was then used to study the post-necking behavior (Hu et al.,2008a; Hu et al.,2008c; Hu et al.,2009). During uniaxial tension, the deformation in the band is extensive and exhibits a large strain gradient due to the geometric constraints at the boundaries between the shear band and the region outside the band. A large rigid body rotation is also experienced. The post-necking behavior of direct-chill (DC) and continuous strip cast (CC) AA5754 alloys has been studied. The relative roles of second phase particles and matrix grain structure have been analyzed systematically by the model and a good explanation is offered for the measured post-necking

behavior and in particular, the differences between materials produced through the CC and DC technologies.

In the meantime, a user material model was developed (Hu et al.,2008c) for the matrix material to consider the grain structure and crystal orientations and their evolution during deformation. In the model, the matrix grains are represented by an isotropic elasto-plastic user material subroutine (VUMAT) for ABAQUS/Explicit but with different relative strengths in terms of their Taylor factors. The Taylor factor and crystal orientations of materials points in grains are updated by a Taylor Bishop Hill (TBH) model coupled in the user material subroutine. This user material model (called the FE-TBH model) has been shown to be a good approximation of a full crystal plasticity model (CP-FEM) in plane strain deformation in terms of strain and Taylor factor contours.

The current paper focuses on the texture and its gradient in the localized necking band seen from the long cross section (RD×ND) by the edge-constrained plane strain model for post-necking deformation. Firstly, the results of the experimental measurements of textures by EBSD of a sample cut along the section are presented. Then the results of the model prediction of grain structure and texture variation are shown and compared with that measured by EBSD.

2 Experimental

A dog-bone shaped (Fig. 1) sample of the as-received AA5754 DC alloy sheet of t_i=2 mm were cut for initial EBSD measurement and uniaxial tensile tests. The EBSD measurements were performed over the normal plane (RD×ND), long cross-section (RD×TD), and short cross-section (TD×ND), respectively. Here the long cross-section is of most interest for our post-necking model and therefore the (111) and (100) pole figures from this cross section are shown in Fig. 2. The calculation of the pole figures and ODF from EBSD measurement is conducted using the MTM-FHM software (Van Houtte,2002) by a Gaussian distribution interpolation in combination with Bunge's series expansion method. The spread used for the Gaussian distribution function is 7^o.

Typical rolling β-fiber texture is identified for this material which runs from Cu (112) <111>, S (123) <634> to Brass (011) <211> components in the Euler space and some weak recrystalization texture with Cube and Goss orientations are also identified.

After fracture by uniaxial tension along the RD direction (Fig. 3(a)), the sample is cut in the middle along the long cross section. The sample is then ground with 240 through 4000 grit SiC paper and mechanically polished with 1 μm diamond and colloidal silica. EBSD measurements are performed at different positions (1-4) of

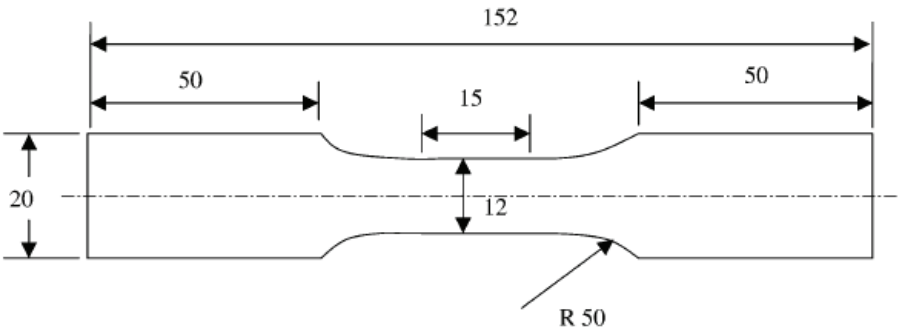

Figure 1: A drawing of the sample geometry for the uniaxial tension test.

the cross sections at or near localized necking area (Fig. 3(b)) using a JSM-7000F FESEM scanning electron microscope equipped with an HKL Technology, Channel 5 system. Standard data noise reduction procedures were employed, including first the reducing of wild spikes, and then noise reduction with 5 neighbors. The EBSD maps with inverse pole figure coloring are as shown in Fig. 4 and the (111) and (100) pole figures of these positions are drawn in Fig. 5. The measurement size of position 1 is 430×320 μm^2. But Fig. 4a shows only the bottom part of the map as the top part had scratches preventing good Kikuchi pattern from being obtained. At this level of deformation there are some areas (shown as green in Fig. 4) where the Kikuchi pattern cannot be indexed and no grain orientation is obtained. The measurement area at position 2 is 570×440gμm^2, while that for the other two positions is 822×620gμm^2.

From the pole figures taken from within the localized necking region, from position 4 to position 1, there are strong (111) and (100) peaks at the North Pole (RD), while the initial textures is rather weak. This means that following deformation the (111) and (100) planes of grains have tended to reorient perpendicular to the rolling direction (RD) or parallel to the short cross section (TD$\times$ND).

3 Methodology

The simulation plane ($x_1\times$ x_2) of the plane strain model is a center cross section of the band. In the initial development, this cross section was assumed to be (RD'$\times$ND) (Hu et al.,2008a), which is perpendicular to the localized band direction (BD). From case of relatively smaller width/thickness ratio where the failure propagates across the width (Fig 3(a)), the section has been modified to be parallel to the long cross-section (RD$\times$ND) (Hu et al.,2009; Hu et al.,2010) of the sample.

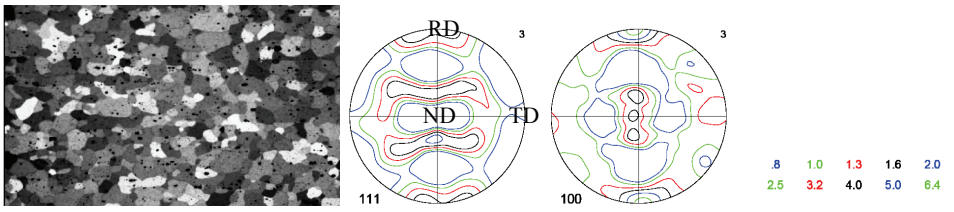

(a) Microstructure (b) Pole figures

Figure 2: Microstructures, pole figures and ODF sections of an AA5754 DC alloy of 2 mm thick calculated from EBSD measurement before uniaxial tension deformation. The contour levels of the pole figure are 0.8, 1.0, 1.3, 1.8, 2.0, 2.5, 3.2, 4.0, 5.0, 6.4. This will apply to all pole figures that appear in the current paper.

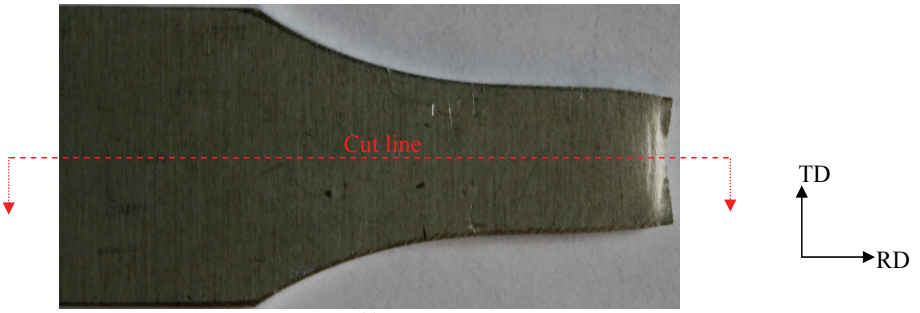

(a)

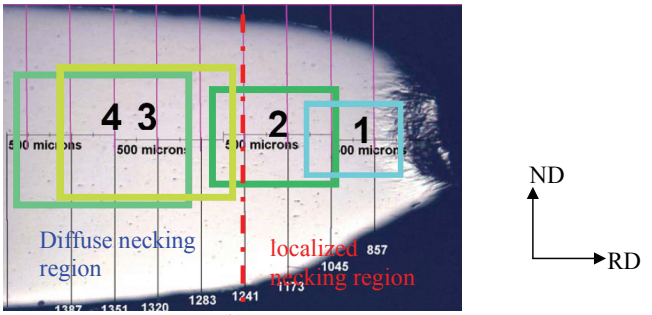

(b)

Figure 3: The fracture sample (a) and the polished long cross section (b) cut from the sample of an AA5754 DC alloy with a initial thickness of 2 mm.

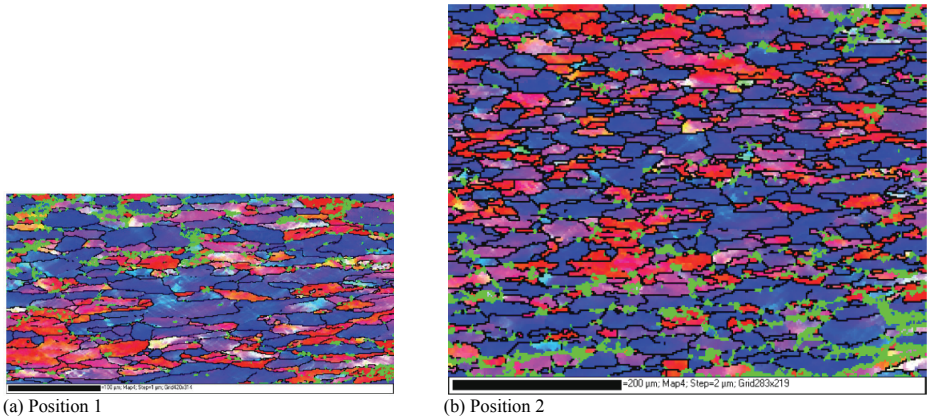

(a) Position 1 (b) Position 2

Figure 4: The EBSD map measurement at the two positions shown in Fig. 3.

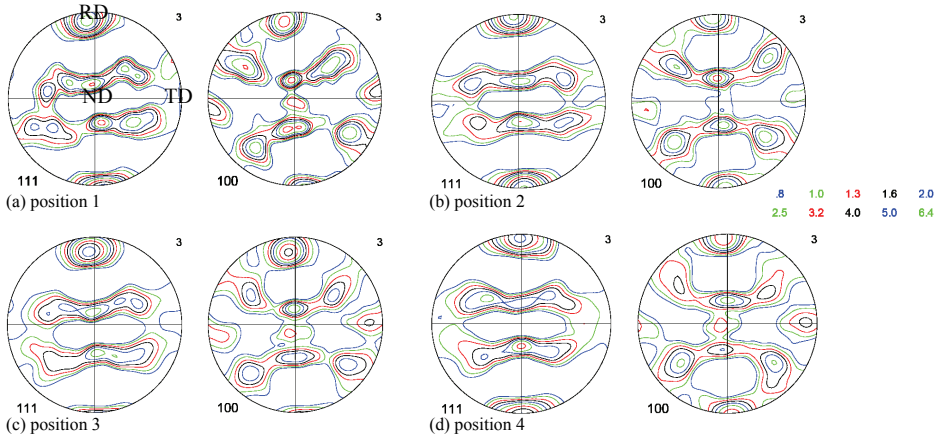

(a) position 1 (b) position 2

(c) position 3 (d) position 4

Figure 5: The (111) and (100) pole figures for the 4 positions shown in Fig. 3.

The deformation is conducted by assigning a velocity (v) along the x_1 (RD) direction to the left (L_e) and right (R_e) edges, while the two edges are constrained along the x_2 (ND) direction (see Fig. 6). The top and bottom edges of the model are free to deform in both degrees of freedom (x_1 and x_2).

The ABAQUS/EXPLICIT finite element software is utilized for the analysis of deformation. An isotropic elasto-plastic rate-independent user material model is used to represent the constitutive behavior of the matrix aluminum alloy (Hu et al., 2008a). In previous work we have used the input flow curve by a three-stage

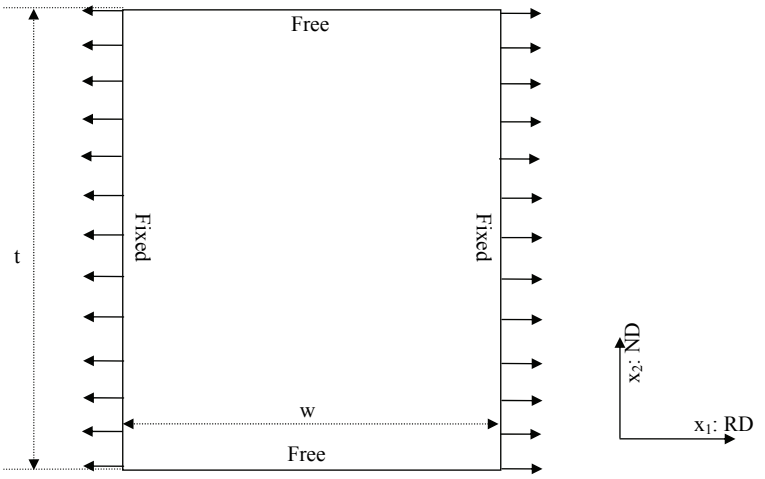

Figure 6: The post-necking model of a initial cross section of a localized necking band (Hu et al.,2008c)

Holloman law (Hu et al., 2008a) based on the fitting of the tensile test results of DC sheet (see Fig. 7).

$$\sigma_y = k_i \varepsilon^{n_i} \tag{1}$$

The fitting parameters are shown in Table 1.

Table 1: Holloman parameters

i	Strain ranges	k_i	n_i
1	$\varepsilon \in$	421.8	0.2613
2	$\varepsilon \in$	570.1	0.3413
3	$\varepsilon \in$	396.6	0.1891

Since this study aims to simulate the post-necking behavior, an initial equivalent strain of ε_0^p=0.36 is assigned to the matrix material, consistent with the assumption that diffuse necking has already occurred before the simulation and a localized neck is about to form (see references (Hu et al.,2009; Hu et al.,2010) for more details).

The methodology for incorporating grain structures, grain orientation and Taylor factor evolution of grains has been detailed elsewhere (Hu et al.,2008c). The result is a user material model called FE-TBH (for "finite element – Taylor Bishop Hill"). The following is a recap of this model.

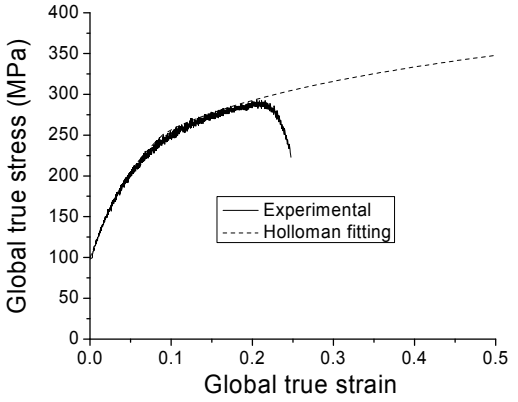

Figure 7: Experimental flow curve and Holloman fitting of the data using parameters in Table 1.

In the FE-TBH model, the initial orientation and Taylor factor of each grain is mapped into each integration point of the finite element model by a modified Voronicell method which uses the grain data measured from EBSD where the grains are simplified as ellipses. For a material integration point **P** in a finite element mesh, the orientation and Taylor factor belonging to one grain orientation are assigned. If we consider the actual 2D spatial distribution of grain orientations measured by EBSD, the choice of orientation is related to the distance (s_{pg}) between each material point $\mathbf{x}_p=\left(x_1^p,x_2^p\right)$ and the center of that grain $\mathbf{x}_g=\left(x_1^g,x_2^g\right)$ which is normalized by the grain size factor D_g as follows.

$$s_{\mathrm{pg}}=\frac{|\mathbf{x}_p-\mathbf{x}_g|}{D_g}=\frac{\left[\left(x_1^p-x_1^g\right)^2+\left(x_2^p-x_2^g\right)^2\right]^{0.5}}{D_g} \tag{2}$$

D_g represents the distance of the center of the ellipse to the intersection point between the ellipse and the connection line of the material point and the ellipse center. For a given material point, the grain orientation with the smallest normalized distance to the point is chosen and assigned to that point. The method of using ellipse simplification will give a closer representation of grain structure generated directly from that of the EBSD measurement points than circular simplification used earlier (Hu et al.,2008a). Furthermore, it offers greater flexibility for different meshes and mesh sizes. The influence of pre-deformation before necking on the initial grain orientations and grain shapes can also be been considered in the model. This is realized by a full constraints Taylor assumption, i.e.,the deformation is homogeneous

everywhere and equal to the macroscopic strain (Taylor,1938). The deformation gradient **F** for uniaxial tension is given by

$$\mathbf{F} = \begin{bmatrix} e^{\varepsilon_0^p} & 0 & 0 \\ 0 & e^{-0.5\varepsilon_0^p} & 0 \\ 0 & 0 & e^{-0.5\varepsilon_0^p} \end{bmatrix} \tag{3}$$

The material point in the configuration ($\mathbf{x}^d$) after pre-deformation is related to the initial material point ($\mathbf{x}$) with no pre-deformation as follows,

$$\mathbf{x}^d = \mathbf{F} \cdot \mathbf{x} \tag{4}$$

To assign a grain orientation to a material point ${\mathbf{x}_p}^d$ in the FE mesh of the configuration with pre-deformation, the coordinates $\mathbf{x}_p$ of this point corresponding to the initial configuration can be calculated by the inversion of equation (4), i.e.,

$$\mathbf{x}_p = \mathbf{F}^{-1} \cdot \mathbf{x}_p^d \tag{5}$$

The calculated coordinates from equation (5) can be used in equation (2) for the selection of grain orientation for this material point.

The relative strength of each grain is represented by a relative Taylor factor (M_g/M). But the material points in each grain are assumed to be isotropic elasto-plastically. In each increment of deformation, the plastic strain increment tensor ($\boldsymbol{\Delta\varepsilon}^p$) of each material point is solved by an isotropic elasto-plastic constitutive law. The displacement gradient $\mathbf{\Delta k}$, i.e. the sum of the calculated plastic strain increment tensor ($\boldsymbol{\Delta\varepsilon}^p$) and the tensor of rigid body rotation increment tensor ($\boldsymbol{\Delta\omega}^R$) provided by the user material interface (VUMAT), is required as an input into the Taylor-Bishop-Hill model developed by Van Houtte et al. (Van Houtte et al.,2005) to update the Taylor factor and lattice orientation of this material point at the end of each increment.

Normally, for a rate-independent Taylor model, the Taylor equation shown below is solved for a grain (g)

$$\Delta\boldsymbol{\varepsilon}^p = \sum \mathbf{P}^\alpha \Delta\gamma^\alpha,\ \mathbf{P}^\alpha = 0.5\,(\mathbf{b}^\alpha \otimes \mathbf{n}^\alpha + \mathbf{n}^\alpha \otimes \mathbf{b}^\alpha) \tag{6}$$

using the minimum work condition

$$\sum \tau_c^\alpha \,|\Delta\gamma^\alpha| = \min \tag{7}$$

$\mathbf{b}^\alpha$ and $\mathbf{n}^\alpha$ are the burgers' vector and slip plane normal of the activated slip system α. The slip increment $\Delta\gamma^\alpha$ of each activated slip system and the Taylor factor of the

grain (M_g) can be calculated by assuming that the critical resolved shear stresses τ_c^α are the same for all slip systems.

$$M_g = \frac{\sum |\Delta\gamma^\alpha|}{\Delta\varepsilon^p} \tag{8}$$

$\Delta\varepsilon^p$ is the equivalent plastic strain increment and equals to $\sqrt{2/3\Delta\boldsymbol{\varepsilon}^p : \Delta\boldsymbol{\varepsilon}^p}$.
The lattice spin ($\Delta\omega^L$), used for upgrading the lattice orientation, can be determined by

$$\Delta\mathbf{k} = \Delta\omega^L + \sum \mathbf{b}^\alpha \otimes \mathbf{n}^\alpha \Delta\gamma^\alpha \tag{9}$$

4 Simulations and results

The simulation is performed with a window size of t×w=1.4×1.2 mm^2 (Fig. 8) which is assumed to be a center cross section of localized necking band just started. The uniform pre-deformation is assumed to be 0.36; therefore the window size prior to uniaxial tension is around 1.67×0.83 mm^2. The grain orientations of material points in the model are assigned by the method described above with consideration of the influence of pre-strain on the shape and crystal orientation of grains. The model has a homogeneous mesh of 350×300 linear plane strain elements with reduced integration. The mesh size of 4 μm is utilized. No damage criterion is used.

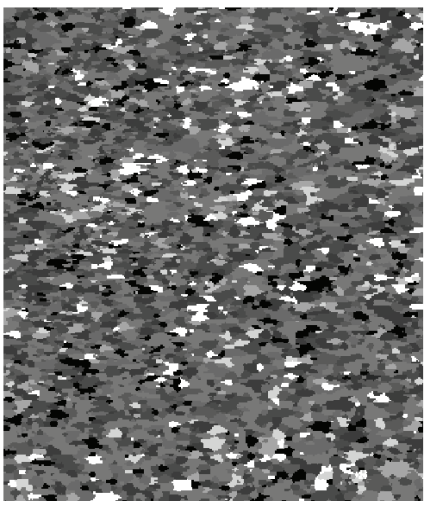

Figure 8: The post-necking model of a initial cross section of 1.4×1.2 mm^2

Fig. 9 shows the (111) and (100) pole figures following pre-deformation of 0.36 using the full constraint Taylor Bishop Hill model. For the purpose of comparison between results, the sample reference frame for the pole figures is chosen to be the same as that of rolling reference frame where x_1=RD, x_2=TD and x_3=ND as shown in Fig. 9(a). But the grain orientations input into the post-necking model is in model reference frame where x_1=RD, x_2=ND and x_3=TD as shown in Fig. 9(b).

The deformed mesh, grain structures and equivalent strain contours after the displacement of one edge of the model reaches 0.432 mm is shown in the Fig. 10. This choice of such a deformation stage is based on the idea that the minimum thickness in reference to the initial thickness is slightly smaller than that of the fractured sample. It can be seen that the deformation is small near the edges, but progresses gradually toward the center of the model where very large deformation is experienced.

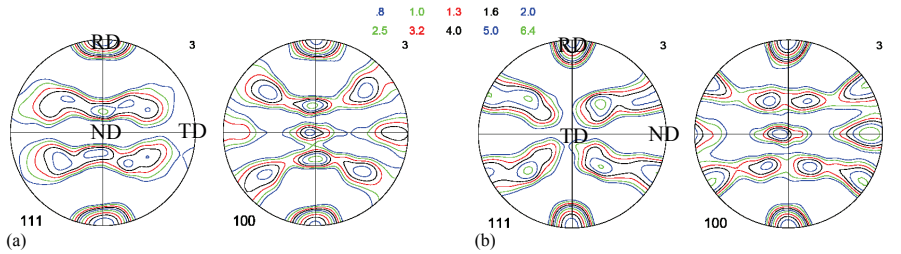

Figure 9: The (111) and (100) pole figures calculated by TBH model with a pre-strain of 0.36 from the texture shown in Fig. 4. The pole figures are drawn in (a) rolling sample reference frame, and (b) model reference frame

The rigid body rotation and lattice spin contours are as shown in Fig. 11. The amount of rigid body rotation $\Delta\alpha_R$ is the angular distance between current material reference frame ($\mathbf{x}$) and the global reference frame ($\mathbf{X}_0$). This is calculated by using the following equation,

$$\Delta\alpha_R = \cos^{-1}\{0.5 \cdot [trace\,(R) - 1.]\} \tag{10}$$

R is the rigid body rotation matrix calculated from the deformation gradient $\mathbf{F}$ and right stretch tensor $\mathbf{U}$ provided by the user material interface (Hu et al.,2008c). It can be seen that the rigid body rotation is greatest close to outer surface and almost none in the center of the model. The maximum rigid body rotation reaches 84^o in Fig. 11(a)

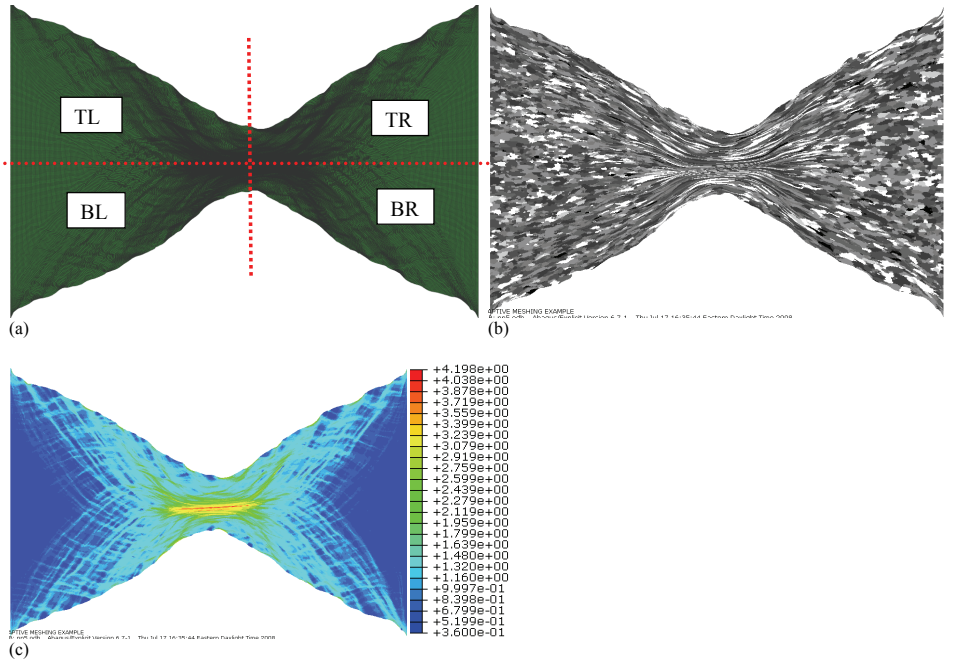

Figure 10: The deformed mesh and grain structures and equivalent strain contours of the post-necking model

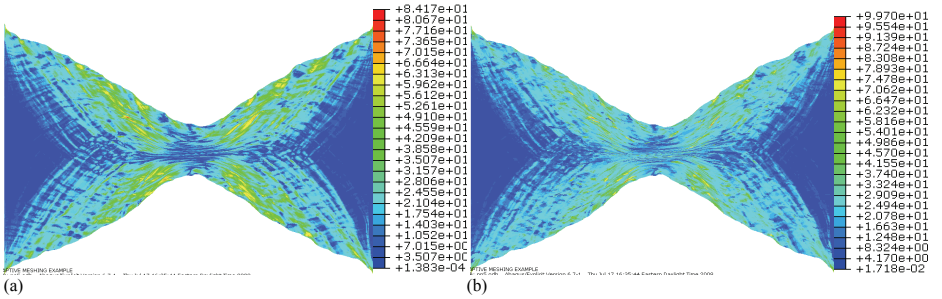

Figure 11: The contours of (a) rigid body rotations; and (b) lattice spins of the post-necking model

The amount of lattice spin $\Delta\alpha_L$ is the angular distance between the current lattice orientation and the initial lattice orientation in reference to the global reference frame ($\mathbf{X}_0$). The maximum rigid body rotation reaches 100^o in Fig. 11(b). The lattice spin in the center of the model is mainly caused by plasticity.

4.1 Symmetry of texture and rigid body rotation

The overall texture of the model is shown by (111) and (100) pole figures in Fig. 12(a). It can be seen that the texture is rather symmetric and it is not surprising considering the effect of global orthorhombic symmetry with the symmetry planes shown as dashed lines in Fig. 10(a).

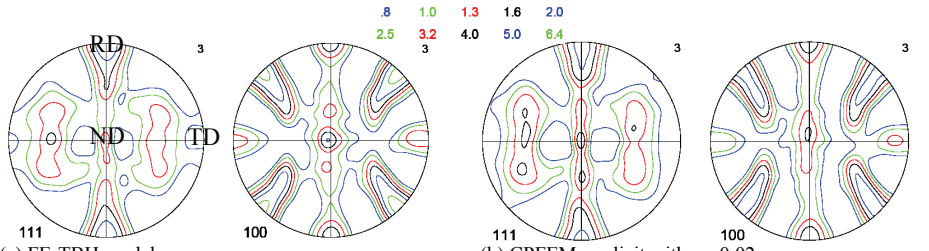

(a) FE-TBH model (b) CPFEM-explicit with m=0.02

Figure 12: The pole figures calculated from the results of the whole model by (a) FE-TBH model and (b) Explicit CPFEM model where rate sensitivity is chosen to be 0.02.

This symmetry, however, does not hold locally. Fig. 13 shows the (111) and (100) pole figures of the four parts divided by the two symmetry planes. The (111) and (100) peaks are shifted always from the north poles (RD) due to rigid body rotation of the various parts around the east pole (TD). Furthermore, the textures are sharper than that of the whole model shown in Fig. 12 which is actually an average of the texture of four parts.

4.2 Texture gradient

4.2.1 Horizontal direction

To show the texture variations along the horizontal direction, the textures of square regions of 200×200 μm^2 delineated in Fig. 14 (the black dashed squares), more specifically Fig. 15 (a), are calculated. Figs. 15(b)-(f) are the (111) and (100) pole figures for regions aligned along the horizontal center-line of the model where the rigid body rotations are smallest. The β-fiber intensity in the Euler space of these locations is shown in Fig. 16. The β-fiber intensity is calculated by using the ODF Skeleton software developed by Delannay (Delannay et al.,2002). It can be shown that the general trend is that the copper and S components get sharper when the location is close to the center of the model where large deformation is experienced. This trend is disturbed by rigid body rotation as shown in Fig. 15(a) at locations C3 and C4 where opposite rigid body rotation tends to randomize the texture. Fig.

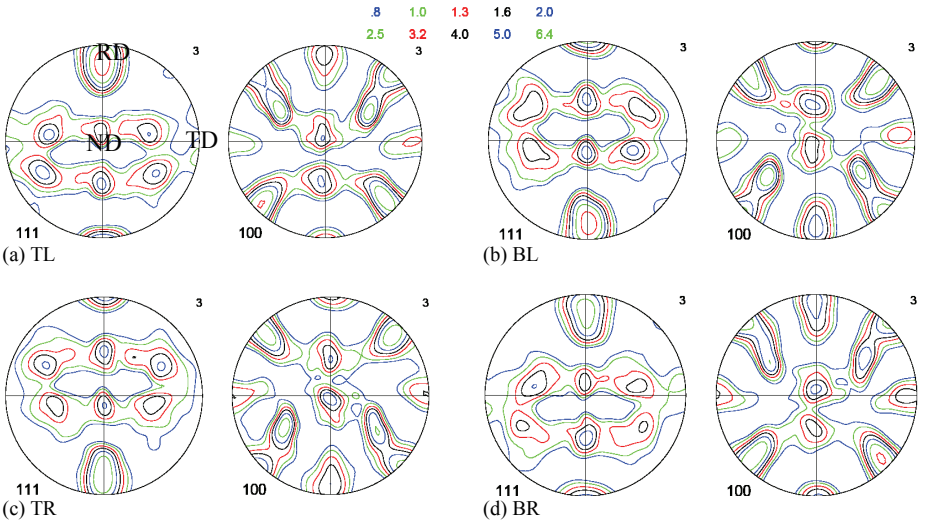

Figure 13: (111) and (100) pole figures of the four symmetric part of the model shown in Fig. 10

16(b) shows the distributions of the rigid body rotation and lattice spin along a narrow band with a width of 4 μm at the horizontal center line of the model.

It is to be noted that that the region with both windows C2 and C3 in Fig. 15(a) (here called window C23) has a similar microstructure to that of the EBSD map of position 1 in Fig. 4(a). The pole figures (Fig. 17) and β-fiber intensity (Fig. 18) of window C23 are found to be similar to that of EBSD measurement. However, the texture is in general a bit weaker than that of the experiment.

4.2.2 Vertical directions

Similar to Fig. 15(a), Fig. 19(a) depicts 5 vertically arranged regions for analyzing their texture distributions. Figs. 19 (b)-(f) are the pole figures for regions of the top-left part of the model. Regions V1-V3 (denoted the LEFT regions) and regions V4-V5 (denoted the RIGHT regions) are arranged along vertical directions which are away from the center with relatively small deformation and close to the center with large deformation, respectively. Fig. 20 shows the distributions of the rigid body rotation and lattice spin along a narrow band with a width of 4 μm at the vertical center line of the LEFT regions (V1-V3). It can be seen that the position of peaks in the pole figures are controlled by rigid body rotations. Regions close to the surface (V1 of the LEFT regions and V4 of the RIGHT regions) exhibit the largest rigid body rotation. In each case, the pole figure has peaks moved considerably

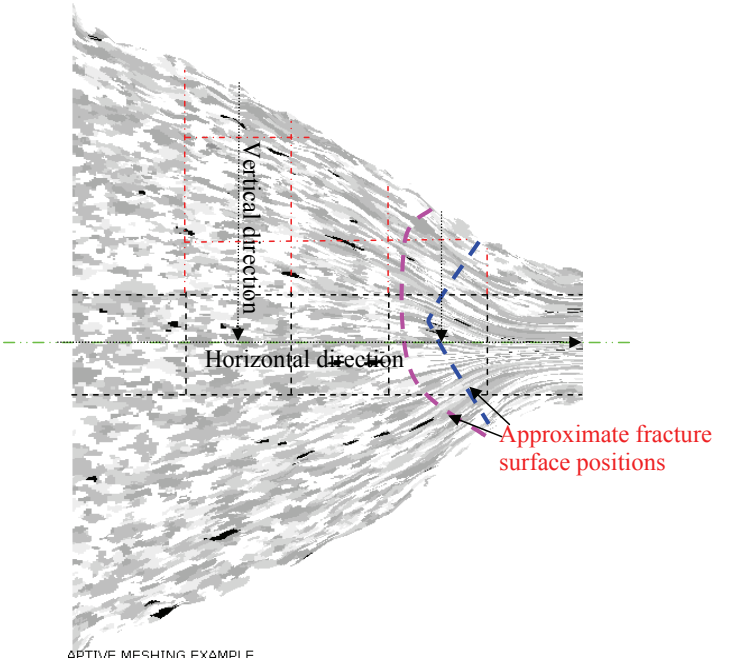

Figure 14: A schematic of regions for texture analysis of horizontal and vertical directions. The pink and blue dashed lines are the approximate cracking locations of a 2 mm thick sample (see Fig. 5) and a 1 mm thick sample (see Fig. 17 in reference (Hu et al.,2008a)), respectively.

away from the sample reference frame axis, such as RD, while the peaks of the region close to horizontal centerline has the least shift. The peak shift of surface part of the RIGHT vertical regions (V4) is more pronounced than that of the LEFT regions (V1) (see Fig. 19(e) and 19(b)).

5 Comparison between FE-TBH and CP-FEM

The FE-TBH model is rather simplified which considers the influence the grain orientations on deformation. Therefore, it is important to know how the prediction of this model compares with a full crystal plasticity model (CPFEM). Based on the viscous CPFEM user subroutine of Huang et al. (Huang,1991) for ABAQUS/IMPLICIT (UMAT) (here called CPFEM-implicit), a user subroutine for ABAQUS/EXPLICIT (VUMAT) was developed (here called CPFEM-explicit) (Hu et al.,2008c). The results of modeling simple shear in a single element model using TBH, FE-TBH, CPFEM-implicit, CPFEM-explicit are almost identical in terms of grain orienta-

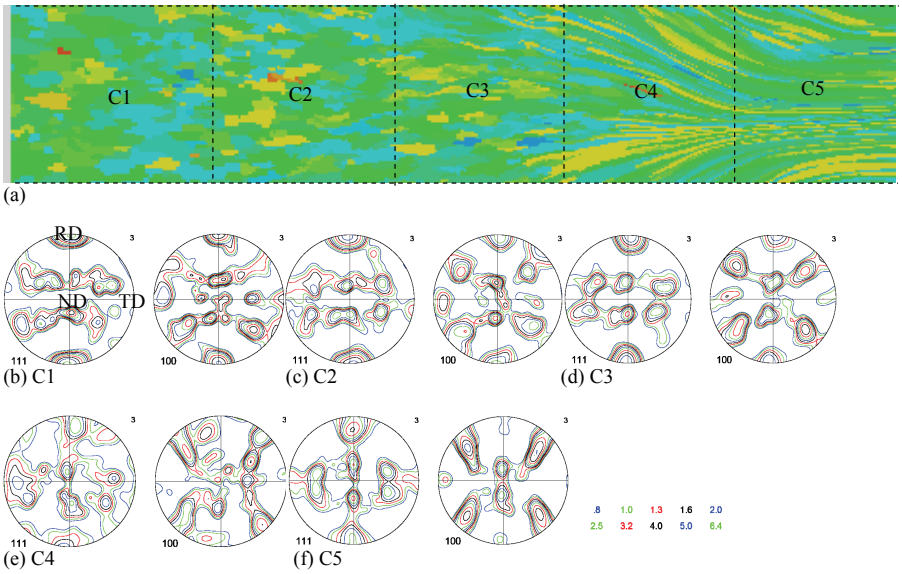

Figure 15: The (111) and (100) pole figures of locations along the center horizontal line of the model

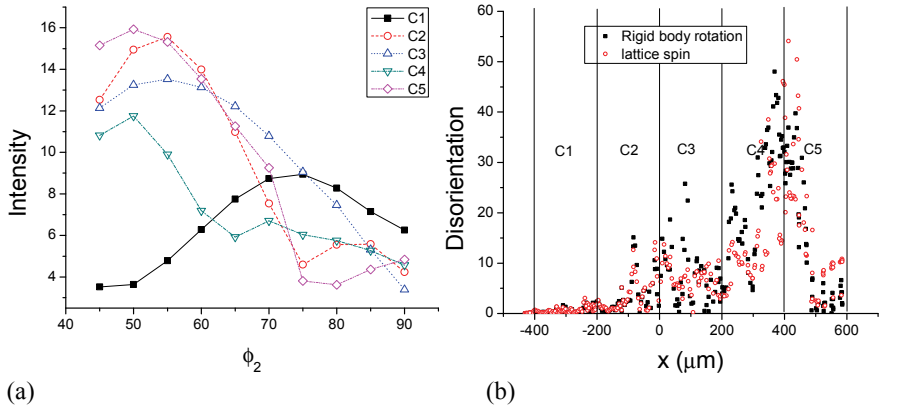

Figure 16: The β-fiber intensity (a) and rigid body rotations (b) of locations along the center horizontal line of the model

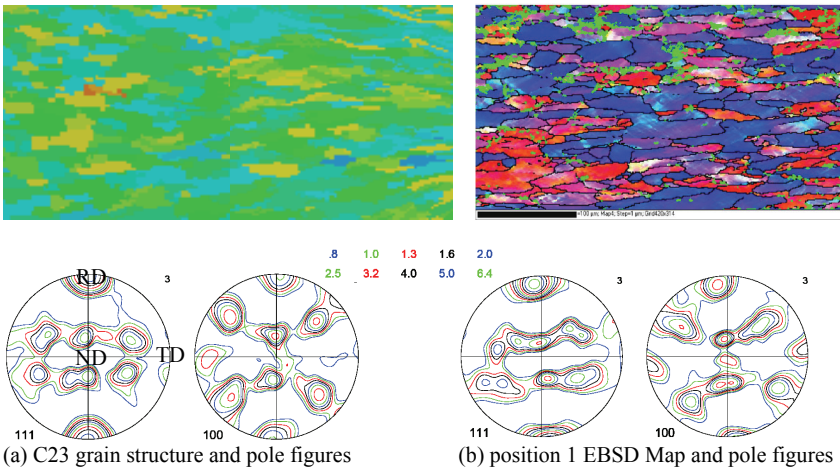

(a) C23 grain structure and pole figures (b) position 1 EBSD Map and pole figures

Figure 17: The grain structure and pole figures of location C23 in FE-TBH model and position 1 of the EBSD measurement.

tion evolution and Taylor factor evolution. The framework of the CPFEM model are described in detail by Huang (Huang,1991) and Kysar (Kysar,2001). Similar to the FE-TBH model, the solutions of the slip increments ($\Delta\gamma^{\alpha}$) of an active slip systems are the key for the calculations of other parameters, e.g. lattice spin, the plastic strain increment and stress increment tensors, etc. In the explicit user material subroutine (CPFEM-explicit), the original rate-tangent modulus formulation is changed into an explicit time integration scheme, where the $\Delta\gamma^{\alpha}$ is obtained directly from the following equation,

$$\Delta\gamma^{\alpha} = \dot{\gamma}_0 sgn(\tau^{\alpha}) \left| \frac{\tau^{\alpha}}{\tau_c^{\alpha}} \right|^{\frac{1}{m}} \cdot \Delta t, \tag{11}$$

where $\dot{\gamma}_0$ is the reference strain rate, τ^{α} and τ_c^{α} are the resolved shear stress and hardness (or called critical resolved shear stress) of the slip system α m and Δt are the rate sensitivity and time increment respectively. The Taylor factor is also calculated from equation (8). Like the CPFEM-implicit, the model convergence rate and stability by the use of CPFEM-explicit is very sensitive to the strain rate sensitivity (m) (Anand et al.,1996). The evolution of critical resolved shear stress is assumed to follow the same Holloman law as in the current FE-TBH model, i.e,

$$\tau_c^{\alpha} = k_i^{\tau} \Gamma^{n_i} \tag{12}$$

with isotropic hardening of each system is assumed, i.e. the critical resolve shear

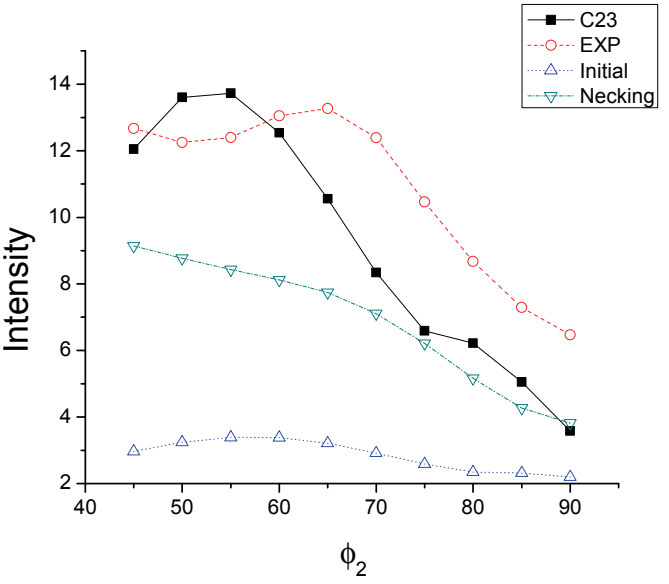

Figure 18: The comparison of the β-fiber intensity of location C23 in FE-TBH model and position 1 of the EBSD measurement at the necking region (Fig. 5) and the initial texture (Fig. 4) and the texture at necking (Fig. 9).

stresses of all systems are the same for a material point in the FE model. Γ is the total slip of all slip systems and

$$k_i^{\tau} = \bar{M}^{-(n+1)} k_i \tag{13}$$

Here $\bar{M}$ is the average Taylor factor of all grains in the model, which is assumed to be constant and equal to 3 in the current work.

The CPFEM-explicit is applied to the current finite element model where the rate sensitivity m and reference strain rate are chosen to be 0.02 and 0.001, respectively.

The equivalent strain contours of the two models when the edges have a displacement u of 0.26 and 0.43 mm are as shown in Fig. 21. As can be seen from the figures, the results are not identical but quite similar in both the locations of large strains and surface roughness. The difference is larger for the model with greater deformation. The (111) and (100) pole figures for the whole model at u=0.43 mm calculated by both FE-TBH and CPFEM-explicit are very close (see Fig. 12). The time used by FE-TBH is 16 hours, while that use by CPFEM-explicit is 100 hours at u=0.43 mm for this model of around 10^5 elements. Although FE-TBH is considerably faster, the CPFEM-explicit code also performs rather well compared with

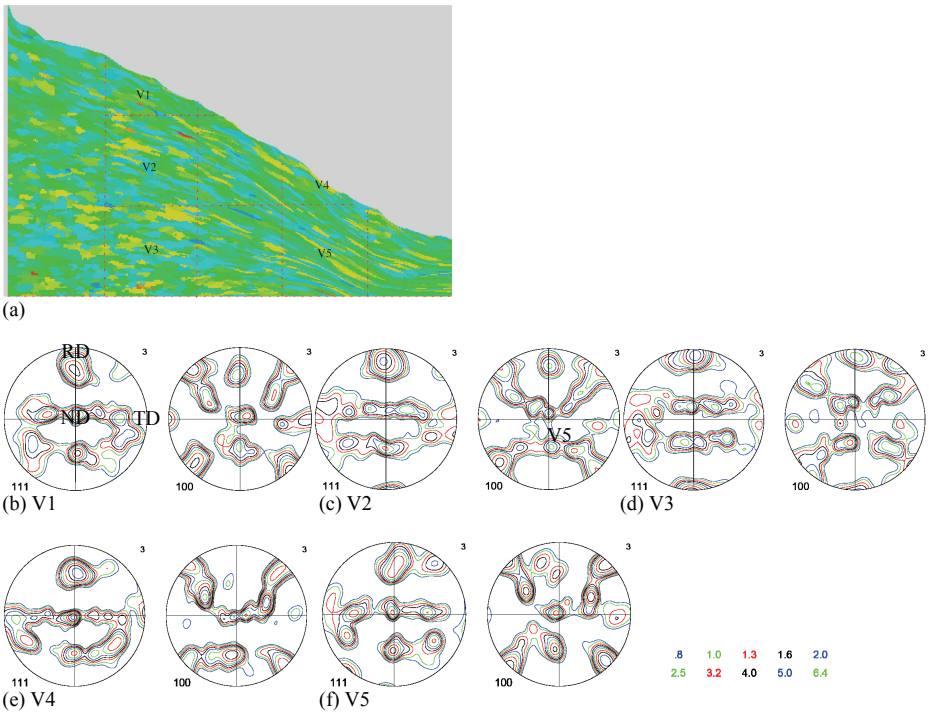

Figure 19: The (111) and (100) pole figures of locations at the top-left position of the model

CPFEM-implicit code which is extremely slow for large models and large deformations.

6 Discussion

The current studies of texture gradient in the localized necking region have shown a good deal of complexity, due to the fact that very large deformation and rigid body rotation are experienced in the region. The deformation has a positive gradient from the two constrained vertical edges toward the center, while the rigid body rotation has a positive gradient from the horizontal center line toward the outer surface. Therefore, the (111) or (100) peaks in the pole figures of outer surface have shifted away from the ideal sample reference axis of the tensile direction which is also the direction of previous rolling (RD). The horizontal centerline is supposed to have little rigid body rotation if the deformation is completely symmetric. But it may not be completely symmetric due to variation of spatial grain distributions.

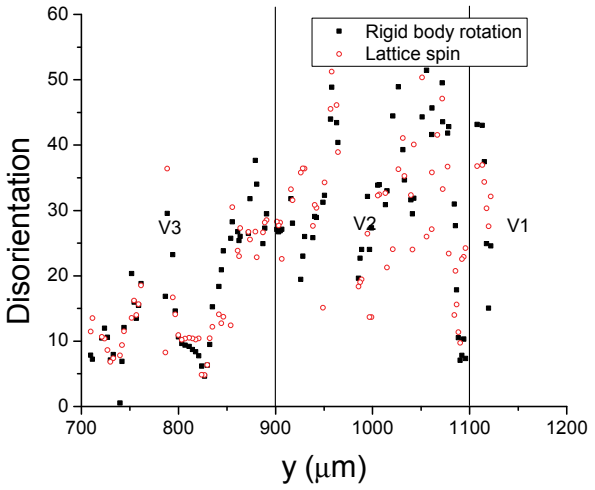

Figure 20: Rigid body rotation at within a band of 4 μm wide around the center line of the left regions (V1-V3)

The deformation gradient has led to increasing Copper and S component intensity along the horizontal centerline, but this trend is disturbed by the variation of rigid body rotation. A rigid body rotation of opposite sign tends to increase the spread of grain orientation, thus randomizing the texture. This helps to explain why the texture of the whole model is considerably weaker compared with the four constituent parts of the model which have symmetry with two perpendicular center symmetry planes. Although the texture of the four constituent parts is not symmetric, the texture of the whole model is, as it is the average. This also explains that the texture at windows C3 and C4 become weaker, although they have larger deformations than windows C1 and C2. The model has shown regions (C2 and C3) which have similar microstructures to that of position 1 very close to the fracture in Fig. 4. The calculated texture from the model is also rather similar to that obtained from EBSD measurement. It therefore appears that the model performs rather well, even though the FE-TBH model contains some significant simplification compared to the full CPFEM model. The FE-TBH model assumes that the material point within matrix grains is isotropic elasto-plastic, but possesses a strength which is related to the Taylor factor of the grain. The Taylor factor and grains are allowed to evolve during deformation using a coupled Taylor-Bishop-Hill model in the user material subroutine. This greatly shortens the calculation time compared with that of full crystal plasticity formulations. This could be very useful in formability predictions in the industry where large scale models with material microstructures input and

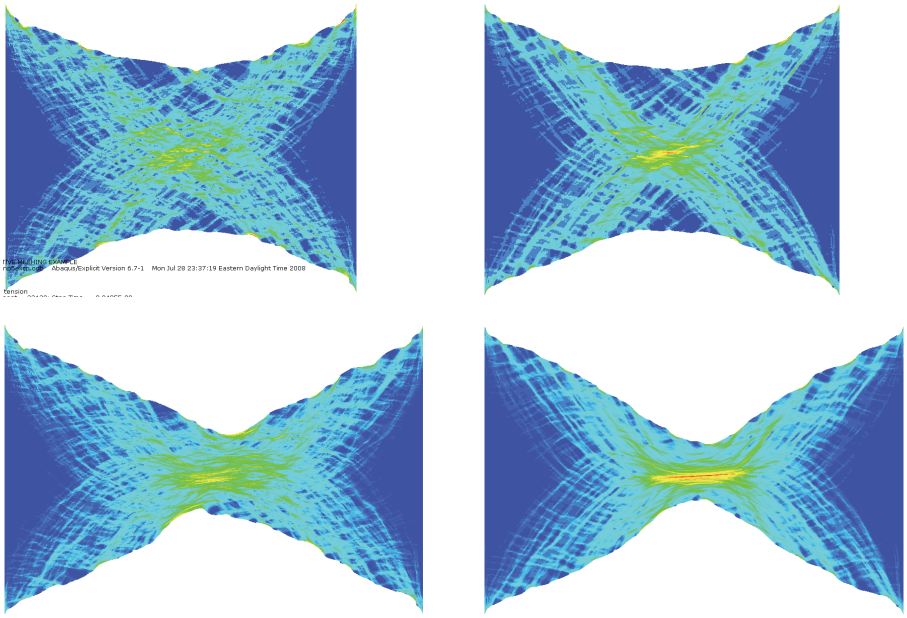

(a) CPFEM-explicit, m=0.02 (b) FE-TBH, rate insensitive

Figure 21: The equivalent strain contours of CP-FEM and FE-TBH models when the displacement of the right edge is 0.26 (the top figures) and 0.43 mm (the bottom figures).

large deformation calculation are involved where the full crystal plasticity calculation is very difficult. It must be noted that the results of the FE-TBH model is quite similar to the CPFEM model in the plane strain calculation where only in-plane (RD$\times$ND) strain anisotropy is allowed where the strains relative to the third direction is zero, but 3D models may show larger differences between these two models. Even the CPFEM model is not that precise when grain size effects such as in the Hall-Petch law are included.

The current studies not only show good correspondence between results of modeling and experiments, but also provide verification of the edge-constraint plane strain model for post-necking deformation proposed by Hu et al (Hu et al.,2008a; Hu et al.,2009). The grain shape variations in the necking region predicted from the model are very similar to that of experiments and corresponding textures are also very close to each other. It must be noted, however, that the real problem is three dimensional, although the 2D post-necking model is a reasonable simplification which captures important features of post-necking deformation. It has been noticed that there is already inhomogeneous through thickness thinning in the long

cross section (RD×ND) in the uniaxial tension test of rectangular cross sectional specimens once diffuse necking starts (see Fig. 3(b) where a tentative line dashed is drawn to divide the sample into two regions: diffuse necking and localized necking regions). There are also variations of thickness if viewed from the short cross section (TD×ND) (Zhang et al.,2001b; Zhang et al.,2001a). These variations of thickness in the long cross section, however, are much smaller and rather gradual compared with that when localized necking band starts. Using a 3D Finite element model of one-eighth of a uniaxial tension sample, Zhang et al. (Zhang et al.,2001b; Zhang et al.,2001a) has tried to determine the true stress-strain curves for uniaxial tension at large strains by analyzing the changes of minimum cross-sectional area. Due to a symmetry boundary condition, it can only be applied to deformation prior to localized necking. By comparing the positions of fracture surfaces in long cross-section of 2 mm (Fig. 3(b)) and 1 mm thick AA5754 DC samples (see Fig. 17 in reference (Hu et al.,2008a)) with that of post-necking model, these positions are approximately drawn in Fig. 14. The maximum equivalent strain of the positions for 2 mm sample is about 2.6, while that for 1 mm is around 3. It must be noted that particles are not considered in the current models due to the rather coarse mesh and they can influence local strain values.

A precise prediction of the pre-necking and post-necking behavior does require a full three dimensional model (Tvergaard,1993). The two dimensional model assumes the microstructure features such as grains or particles extend from one surface to the other. This amplifies the inhomogeneities of these features. Unlike the plane stress model of RD×TD plane where the variation of through-thickness strains is overestimated (Hu et al.,2008a; Hu et al.,2007; Hu et al.,2008b), the strain of the third direction of the plane strain model (TD) is zero which may overestimate the stress variations. A full three-dimensional study is not tractable with microstructure inputs of realistic uniaxial tension sample with ordinary grain and particle sizes in AA5754 alloys. In the future, however, a coarse meshed three-dimensional model with some imperfections will be studied to provide a more comprehensive understanding of the deformation sequences. This will help to develop more refined two dimensional models that can be proposed for microstructure-based finite element studies.

7 Conclusions

A microstructure-based plane strain model based on an FE-TBH user material subroutine has shown rather good predictions of grain structure variations in the post-necking region in comparison with EBSD data, which show slightly elongated grains that become more elongated towards the center of the model. The predicted texture from FE modeling of a window that has similar shapes and shape varia-

tions of grains with that experimentally observed from a region (position 1 in Fig. 5) mostly close to the fracture surface is similar to the texture calculated from the measured EBSD orientation map of the region (Fig. 6(a)). The texture gradient in the post-necking region is related to rigid body rotation induced by geometric constraint. In general the Copper and S component become sharper from edge to center, but this is disturbed by rigid body rotation which tends to randomize the texture. Largest rigid body rotation is in the outer surface which makes the (111) and (100) peaks shift away from the ideal RD direction.

Acknowledgement: This work is supported by General Motors (GM) of Canada and National Science and Engineering Research Council of Canada (NSERC)

References

Anand, L., Kothari, M. (1996): A computational procedure for rate-independent crystal plasticity, Journal of the Mechanics and Physics of Solids 44, 525-558.

Bate, P. (1999): Modelling deformation microstructure with the crystal plasticity finite-element method, Philosophical Transactions of the Royal Society of London Series A-Mathematical Physical and Engineering Sciences 357, 1589-1601.

Becker, R. (1991): Analysis of texture evolution in channel die compression .1. Effects of Grain Interaction, Acta Metallurgica et Materialia 39, 1211-1230.

Becker, R. (1992): An Analysis of Shear localization during bending of a polycrystalline sheet, Journal of Applied Mechanics-Transactions of the Asme 59, 491-496.

Bronkhorst, C. A., Hansen, B. L., Cerreta, E. K., Bingert, J. F. (2007): Modeling the microstructural evolution of metallic polycrystalline materials under localization conditions, Journal of the Mechanics and Physics of Solids 55, 2351-2383.

Delannay, L., Jacques, P. J., Kalidindi, S. R. (2006): Finite element modeling of crystal plasticity with grains shaped as truncated octahedrons, International Journal of Plasticity 22, 1879-1898.

Delannay, L., Kalidindi, S. R., Van Houtte, P. (2002): Quantitative prediction of textures in aluminium cold rolled to moderate strains, Materials Science and Engineering A 336, 233-244.

Hu, X. H., Gasperini, M., Van Houtte, P. (2005a): Strain localization observed during shearing of some aluminium alloys and texture softening predicted by FC Taylor and Adavanced Lamel Model, Solid State Phenomena 105, 363-370.

Hu, X. H., Gasperini, M., Van Houtte, P. (2005b): Texture prediction of an AA3004 aluminum alloy with the occurrence of strain localization during simple shear using a multiscale modeling procedure, Materials Science Forum 495-497,

1103-1110.

Hu, X. H., Jain, M., Wilkinson, D. S., Mishra, R. K. (2008a): Microstructure-based finite element analysis of strain localization behavior in AA5754 aluminum sheet, Acta Materialia 56, 3187-3201.

Hu, X. H., Wilkinson, D. S., Jain, M., Mishra, R. K. (2009): The influence of particle shape, volume fraction and distribution on post-necking deformation and fracture in uniaxial tension of AA5754 sheet materials, International Journal of Solids and Structures 46, 2650-2658.

Hu, X. H., Wilkinson, D. S., Jain, M., Mishra, R. K. (2010): A parametric finite element study and an analytical model of particle distributions on post-necking deformation and failure mode in AA5754 aluminum alloy sheets, International Journal of Fracture In press, DOI:10.1007/s10704-010-9466-9.

Hu, X. H., Wilkinson, D. S., Jain, M., Mishra, R. K. (2008b): Modeling strain localization using a plane stress two -particle model and the influence of grain level matrix inhomogeneity, Journal of Engineering Materials and Technology - Transactions of the ASME 130, Paper No. 021002.

Hu, X. H., Wilkinson, D. S., Jain, M., Mishra, R. K. (2007): Modeling the influence of grain-level matrix inhomogeneity on strain localization in the presence of hard particles, Modelling and Simulation in Materials Science and Engineering 15, 893-909.

Hu, X. H., Wilkinson, D. S., Jain, M., Wu, P. D., Mishra, R. K., Kim, S., Sachdev, A. K. (2008c): The role of textures and particles on post-necking deformation in AA5754 alloys, Submitted

Huang, Y. (1991): A User-Material Subroutine Incorporating Single Crystal Plasticity in the ABAQUS Finite Element Program, MECH 178.

Kalidindi, S. R., Bronkhorst, C. A., Anand, L. (1992): Crystallographic Texture Evolution in Bulk Deformation Processing of Fcc Metals, Journal of the Mechanics and Physics of Solids 40, 537-569.

Kysar, Jeffrey W. (2001): Continuum simulations of directional dependence of crack growth along a copper/sapphire bicrystal interface. Part I: experiments and crystal plasticity background, Journal of the Mechanics and Physics of Solids 49, 1099-1128.

Lebensohn, R. A., Tome, C. N. (1993): A Self-Consistent Anisotropic Approach for the Simulation of Plastic-Deformation and Texture Development of Polycrystals - Application to Zirconium Alloys, Acta Metallurgica et Materialia 41, 2611-2624.

Leffers, T., Vanhoutte, P. (1989): Calculated and Experimental Orientation Distributions of Twin Lamellae in Rolled Brass, Acta Metallurgica 37, 1191-1198.

Li, S., Hoferlin, E., Van Bael, A., Van Houtte, P. (2001): Application of a texture-based plastic potential in earing prediction of an IF steel, Advanced Engineering Materials 3, 990-994.

Taylor, G. I. (1938): Plastic strain in metals, Journals of the Institute of Metals 62, 307.

Tvergaard, V. (1993): Necking in Tensile Bars with Rectangular Cross-Section, Computer Methods in Applied Mechanics and Engineering 103, 273-290.

Van Houtte, P. (2002): MTM-FHM software.

Van Houtte, P., Li, S. Y., Seefeldt, M., Delannay, L. (2005): Deformation texture prediction: from the Taylor model to the advanced Lamel model, International Journal of Plasticity 21, 589-624.

Wu, P. D., Lloyd, D. J. (2004): Analysis of surface roughening in AA6111 automotive sheet, Acta Materialia 52, 1785-1798.

Wu, P. D., Lloyd, D. J., Bosland, A., Jin, H., MacEwen, S. R. (2003): Analysis of roping in AA6111 automotive sheet, Acta Materialia 51, 1945-1957.

Wu, P. D., Lloyd, D. J., Jain, M., Neale, K. W., Huang, Y. (2007): Effects of spatial grain orientation distribution and initial surface topography on sheet metal necking, International Journal of Plasticity 23, 1084-1104.

Yoon, J. W., Yang, D. Y., Chung, K., Barlat, F. (1999): A general elasto-plastic finite element formulation based on incremental deformation theory for planar anisotropy and its application to sheet metal forming, International Journal of Plasticity 15, 35-67.

Zhang, Z. L., Odegard, J., Sovik, O. P. (2001a): Determining true stress-strain curve for isotropic and anisotropic materials with rectangular tensile bars: method and verifications, Computational Materials Science 20, 77-85.

Zhang, Z. L., Odegard, J., Sovik, O. P., Thaulow, C. (2001b): A study on determining true stress-strain curve for anisotropic materials with rectangular tensile bars, International Journal of Solids and Structures 38, 4489-4505.